Research Article

Novel Homogeneous Anion Exchange Membranes for Reproducible and Sensitive Nucleic Acid Detection via Current–Voltage Characteristic Measurement

Jie-Ning Chuang, Pei-Yin Diao, Wen-Shan Huang, Li-Fen Huang, Satyajyoti Senapati, Hsueh-Chia Chang, and Yi-Ming Sun*

ACCESS | 📊 Metrics & More | 📰 Article Recommendations | 🆂🅸 Supporting Information

ABSTRACT: One-pot synthesis of novel hydrogel-based anion exchange membranes (AEMs), with only a single-phase monomer mixture, was used to eliminate surface heterogeneity and generate reproducible electroconvective microvortices in the over-limiting region of the current−voltage characteristic (CVC) curves. Diallyldimethylammonium chloride (DDA) was used as the main component to provide the cation charge groups, and 2-hydroxyethyl methacrylate (HEMA) and ethylene glycol dimethyl acrylate (EGDMA) were used as the auxiliary structure monomers. The uniform membrane structure allowed reproducible and sensitive DNA detection and quantification, as probe−target surface complexes can gate the ion flux and produce large voltage shifts in the over-limiting region. Suppressed membrane curvature due to controlled swelling is a crucial part to avoid the reduction of depletion region for maintaining the influence of target gene hybridization. Fourier-transform infrared (FTIR) spectroscopy verified the synthesized membrane structure, with a residual vinyl group that allows easy carboxylation via additional photografting reaction. Consequently, a significantly higher DNA probe functionalization efficiency is obtained on the homogeneous AEMs, evidenced by the increasing nitrogen element content and bonding via X-ray photoelectron spectroscopy (XPS). The DDA content was optimized to provide a sufficient coulomb force between AEM and nucleic acid backbone to promote the specific binding efficiency but without high dimensional swelling which might change the surface geometry and restrict the voltage shifting for sensing in the over-limiting region, and the optimal DDA/HEMA ratio was found to be 4/10. The synthesized AEM sensor for recombinant 35S promoter sequence identification exhibited a reproducible calibration standard curve with dynamic range between 30 fM and 1 μM and high selectivity with only 0.01 V shift for 1 μM nontarget oligo.

KEYWORDS: current−voltage characteristic, anion exchange membrane, biosensor, microfluidics, GMO
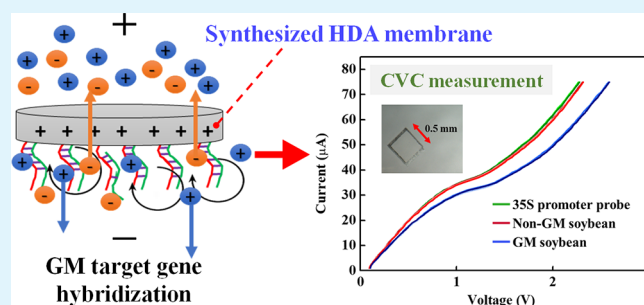
INTRODUCTION

Probe-based sequence-specific nucleic acid detection has wide applications in clinical diagnosis, environmental monitoring, and food industry.[1−3] While profiling microRNA over-expression and detection of mutations in mRNAs are promising screening tests for many diseases, particularly cancer, DNA remains the most robust detection target for pathogen (bacteria/virus) diagnostics and for genetically modified (GM) crops. This is because the stability of the double helix can prevent DNA rapid degradation compared to the relatively fragile RNAs.[4,5] Although only ten copies of the DNA templates are needed for detection and quantification by quantitative polymerase chain reaction (qPCR), the qPCR instrument is expensive and bulky because of the requisite fluorescence-based optics,[6] not to mention costly reagents. As a consequence, there is a need for an affordable, reliable, and straightforward method to convert the probe-DNA hybrid-

ization into a signal perceivable by low-cost detectors without expensive molecular optical reporters.[7,8] In our research, the recombinant 35S promoter in GM soybean was used as an example for nucleic acid identification. This viral 35S promoter is commonly applied to constitutively activate the transcription of the recombinant genes such as herbicide-resistant EPSPS (5-enolpyruvylshikimate 3-phosphate synthase) and various insect-resistant Bt (*Bacillus thuringiensis*) in transgenic soybean.[9,10]
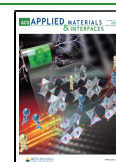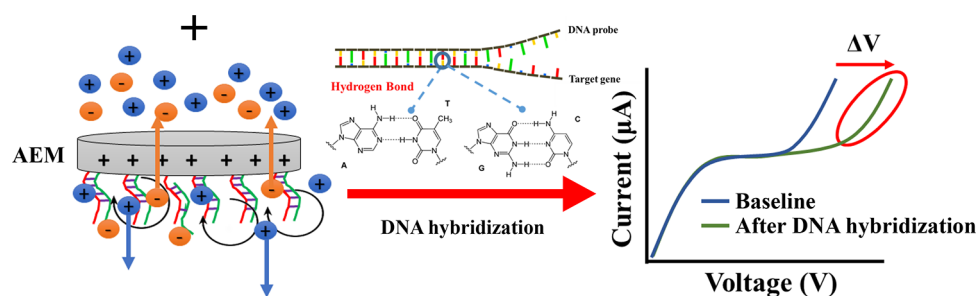
Figure 1. Principle of voltage shift after target gene hybridization. The micro-hydrodynamic environment of the vicinity of the AEM surface with the probe changes after target gene hybridization and retards the formation of microvortices for the further transport of anions from the bulk to the membrane surface. Therefore, the total resistance across the membrane increases, and a larger voltage (ΔV, voltage shift) is needed for the same current flow in the over-limiting region.

There are several biosensors reported for GM crops detection. Qiu et al. reported a novel fluorescent biosensor through the hybridization between the fragments of 35S promoter and G-quadruplex DNA probes to increasing a strong fluorescence for target DNA classification, and their detection limit could reach 2 nM.[11] Fortunati et al. demonstrated that an amperometric sandwich-format geno-sensor enhanced by single-walled carbon nanotube screen printed electrodes (SWCNT-SPEs) could be used in non-amplified soybean genomic DNA detection, and their sensing limit was 64 pM in oligonucleotide detection.[12] Sun et al. developed an electrochemical biosensor for 35S promoter identification. When the oxidative dissolution of lead sulfide particles was triggered by the hybridization of mercaptoacetic acid-modified PbS particles and target DNA fragments, the free lead ion can be monitored by anodic stripping voltammetry (ASV). The detection limit of target DNA was ~4.38 pM.[13] Although these label-free and PCR-free biosensors had a high sensitivity, they still suffer from long incubation time, expensive sensor, sample and equipment costs, and multistep operation that are not suitable for point-of-care (POC) applications.

Recently, an anion exchange membrane (AEM)-based ionic current nucleic acid sensing technology has been pro-posed.[14,15] It utilizes electrophoresis toward the membrane to reduce the assay time and is extremely low cost. The central signal amplification concept of this technology relies on the current–voltage characteristic (CVC) behavior.[16−20] When the target gene is electrophoretically directed toward the AEMs and hybridize with the surface functionalized probes, the hybridization complexes are shown to reduce the development of microvortices near the membrane surface.[21] These micro-vortices convect bulk ions into the ion depleted region at the membrane surface and is responsible for the transition from the limiting-current region to the overlimiting current region in the CVC. The surface field due to the hybridized complex, which are oppositely charged from the AEM, suppresses the electroconvective instability responsible for the mixing micro-vortices. The theoretically infinite differential resistance in the limiting region is due to near-DI ionic strength in a small neighborhood, within 100 nm (Debye thickness for DI water), of the membrane surface. Hence, if microvortices cannot replenish ions into this small region, the resistance of the over-limiting region would be significantly amplified because by a small number of surface target molecules. Therefore, a significant voltage shift of the overlimiting CVC can be observed in the positive-control sample with a small number of

nucleic acids on the membrane surface, in comparison to a nontarget sample, in Figure 1.

This membrane sensing technique has made significant progress in the past few years. Lower detection limit is shown to be in the picomolar range for oligonucleotide.[14] Slouka et al.[22] showed that water splitting due to an effective bipolar membrane that forms when there is an excessive assembly of the target DNA imposes the upper limit of micromolar. Moreover, the membrane sensor can be easily assembled into a microfluidic chip. A carefully metered hydrodynamic shear force, created by the flow of a PBS wash solution, was applied to remove the nonspecifically bound nucleic acids from the membrane surface to improve specificity. Controlled shear flow leading to a reproducible steady-state CVC signal has been shown in related probe-based assay to achieve two-mismatch discrimination of nontargets.[23,24] Ramshani et al. further demonstrated the integrability of the AEM sensor by integrating it with a surface acoustic wave (SAW) lysing module and a cation exchange membrane analyte concen-tration component. Untreated extracellular vesicles (exo-somes) could be lysed and their microRNA concentrated and detected at the same channel within 30 min.[25] However, a bottleneck limits the intersensor reproducibility of the CVC signal such that the individual sensors need to be calibrated. This shortcoming has prevented widespread application and commercialization of this sensor technology. The commercial AEMs used in previous studies were heterogeneous as they were made of fibrous supports and anion exchange resin beads.[14,22,25] Periodically spaced heterogeneities are known to significantly affect the over-limiting current.[26−28] The irregular heterogeneities on the commercial membranes are expected to trigger electroconvective instabilities of different amplitude and further produce irreproducible CVCs. Consequently, there is a need to synthesize heterogeneity-free membrane sensors that can generate reproducible electroconvection and enable possible quantification of DNA targets with a universal standard curve, which greatly broadens the application range of this technology.

In this work, a hydrogel-based AEM sensing assembly platform was proposed to eliminate the heterogeneity by curing without any fabrics or randomly packed resin granules. There are several common methods for homogeneous membrane preparation, such as free-radical polymerization,[29] polycondensation,[30,31] and charge group modification.[32] We adopted a method similar to that for contact lens fabrication and directly photopolymerized with quaternary amine monomer in a one-pot reaction to avoid the tedious

Table 1. Chemical Formulation of Various HDA Membranes and Commercial Ralex Membrane

	HDA-3	HDA-4	HDA-5	HDA-6	Ralex membrane
DDA/HEMA (v/v)	3/10	4/10	5/10	6/10	
charge carrier (DDA, mmol)	0.12	0.16	0.20	0.23	$(R-(CH_3)_3N^+)$
cross-linker (EGDMA, mmol)	0.01	0.01	0.01	0.01	PES (fitting fabrics)
monomer (HEMA, mmol)	0.85	0.85	0.85	0.85	PE (binder)

quaternization steps and conversion variation using tertiary amine monomers.[33] Therefore, a transparent hydrogel membrane with quaternary amine groups could be obtained within a short exposure time to UV light. The membrane exhibited not only a typical CVC behavior but also had less variation on the slope in each region due to its uniform structure and a convex geometry effect to be described later. The residual vinyl groups in the newly developed membranes also allow probe functionalization by carboxylation, leading to a better probe immobilization efficiency. With the self-synthesized membranes, simple reactive functional groups in the AEM make the membrane surface more easily react with a predesigned DNA probe. This procedure would allow future studies to identify nucleic acid more effectively. Consequently, this newly developed hydrogel sensing element integrated microfluidic-based diagnostic platform could serve as a promising tool in nucleic acid detection in a rapid, reproducible, and sensitive fashion. We validate the reproducibility and enhanced sensitivity/dynamic range of the new membrane sensor by detecting specific DNAs related to GM soybeans.

■ EXPERIMENTAL SECTION

Materials and Reagents. A heterogeneous Ralex membrane composed of quaternary amine, supported by polyethylene binder and polyamide/polyester fitting fabrics, was purchased from MEGA a. s., Czech. A Sylgard 184 silicone elastomer kit from Dow Corning Corp. and Quik-cast polyurethane casting resin from TAP Plastic Inc. were applied in sensor fabrication. For homogeneous AEM preparation, 2-hydroxyethyl methacrylate (HEMA, 97%) from Acros Organics, ethylene glycol dimethyl acrylate (EGDMA, 98% with 100 ppm 4-methoxylphenol) from Alfa Aesar, diallyldimethylammonium chloride (DDA, 60% in water) from TCI, and 2-hydroxy-2-methyl-propiophenone (Irgacure 1173) photoinitiator from BASF SE were used. The 10× phosphate-buffered saline (10× PBS) which contains 27 mM potassium chloride, 14.7 mM potassium dihydrogen phosphate, 1.37 M sodium chloride, and 77 mM disodium hydrogen phosphate buffer, pH 7.4, was from Uniregion Bio Tech Inc. The 50× TAE buffer that contains Tris base, acetic acid, and EDTA, 3-(ethyliminomethyleneamino)-N,N-dimethyl-propan-1-amine (EDC), benzophenone-3,3,4,4-tetracarboxylic acid, 2-(N-morpholino)-ethanesulfonic acid (MES), and sodium hydroxide were purchased from Sigma-Aldrich. The genomic DNA Mini Kit (Plant) GP100 was obtained from Geneaid Biotech Ltd. SsoAdvanced Universal SYBR Green Supermix from BIO-RAD, DM-2100 (DNA ladder) and FluoroVue nucleic acid gel stain (10000×) from Smobio Technology, Inc., and agarose LE from MDBio, Inc., were used for preparation of DNA electrophoresis. All customized oligonucleotides were ordered from Integrated DNA Technologies, Inc., with the following sequences: 5′-/5AmM/C12/CCC ACT ATC CTT CGC AAG ACC (amine-ended DNA probe), 5′-GGT CTT GCG AAG GAT AGT GGG (target DNA oligo), 5′-ATT GAT GTG ATA TCT CCA CTG ACG T (forward primer), 5′-CCT CTC CAA ATG AAA TGA ACT TCC T (reverse primer), and 5′-CGT CGC GGT GAG TTC AGG CT (nontarget DNA oligo, sequence outside the target region in 35S promoter). Negative and positive soybean samples in tests were obtained randomly from a local market in Taiwan.

Soybean Genomic DNA Extraction and PCR Amplification. Soybean seeds were frozen in liquid nitrogen and ground to a fine powder. About 100 mg of soybean powder was used for genomic DNA extraction according to the manufacturer's instruction by the plant genomic DNA mini kit (Geneaid, New Taipei City, Taiwan). The target DNA was amplified from 100 ng/μL of template genomic DNA in a final 20 μL polymerase chain reaction (PCR) solution (SsoAdvanced Universal SYBR Green Supermix, Biorad, USA) by using a DNA thermal cycler (Bio-Rad Laboratories, Inc., T100 thermal cycler). After preheating at 95 °C for 30 s, 35 amplification cycles were performed at 95 °C for 10 s, 58 °C for 30 s, and 72 °C for 40 s. The final incubation was performed at 72 °C for 5 min. The amplified 101 bp of 35S promoter DNA fragments were examined by 1.5% agarose gel electrophoresis (Figure S1, Supporting Information).

Membrane Preparation. The homogeneous quaternary amine AEMs were directly prepared from a mixture solution of various compositions of diallyldimethylammonium chloride (DDA), 2-hydroxyethyl methacrylate (HEMA), ethylene glycol dimethyl acrylate (EGDMA), and a trace amount of Irgacure 1173 (photoinitiator). The chemical formulation of various synthesized membranes along with the commercial Ralex membrane are shown in Table 1. The photoinitiated polymerization was adopted because it is a well-known technique to prepare polymer materials from vinyl monomers.[34] In this work, we had tried different ratios of EGDMA up to 10 mol % to enhance the mechanical stability in PBS solution; however, the AEMs became fragile and easily broken, even increasing the EGDMA content during the swelling tests. Consequently, the EGDMA content was fixed at 1 mol %. The crucial part of AEMs is the content of quaternary amine in the hydrogel; it not only increases the ion exchange capacity (IEC) but also affects the degree of swelling and dimensional stability of the membranes in the PBS solution. Therefore, the effect of DDA/HEMA ratio on the membrane properties was explored in this study.

A silicone frame of 0.5 mm in thickness was pinched between two-level release films and glasses to form a sandwich-type mold; the monomer solution was injected into the mold and then directly cured via photoinitiated polymerization in the mold with a UV energy density of 30 mW/cm² at 356 nm wavelength for 25 min. The obtained homogeneous DDA-based AEMs (named HDA membranes) presented a transparent and smooth surface with 0.5 mm of controlled thickness. At the final step, AEMs were stored in 0.1× PBS buffer, pH 7, to achieve the swelling equilibrium until DNA probe attachment or CVC testing.

Sensor Fabrication. Both commercial membrane and HDA membranes were cut into 0.5 × 0.5 mm² squares and placed on the silicone mold for sensor head fabrication. The membrane could be embedded in the polyurethane resin frame after curing at room temperature. The membrane sensor heads were preserved in 0.1× PBS buffer, pH 7, at least 24 h before tests or surface modification. The sensor head has an opening of 0.25 mm² through which the membrane is exposed to the DNA solution.

DNA Probe Functionalization onto the Membrane Surface. A two-step functionalization protocol was performed to immobilize DNA probe on the membrane surface. The AEM sensor head was carboxylated first for a later EDC coupling step with amine-ended DNA probe. The carboxylic reagent was prepared by adding 2 mg of 3,3,4,4-benzophenonetetracarboxylic acid in 50 μL of deionized water, and the pH was adjusted to 7 by adding sodium hydroxide solution.[35] To create carboxylic acid groups (−COOH) on the membrane surface, 20 μL of carboxylic reagent was dropped on the AEM surface and exposed to UV light for 20 min. The carboxylated membrane sensor head was stabilized in 0.1× PBS buffer, pH 2, and then preserved in 0.1× PBS buffer, pH 7. Next, the carboxylated membrane
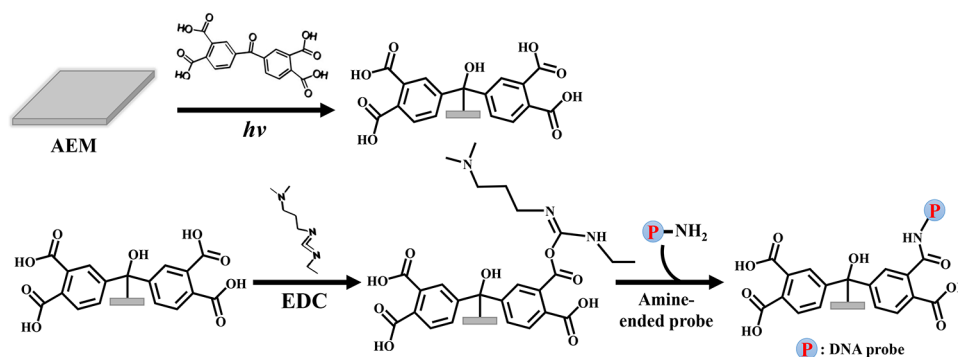
Figure 2. Reaction scheme of the two-step DNA probe functionalization on the surface of AEMs.
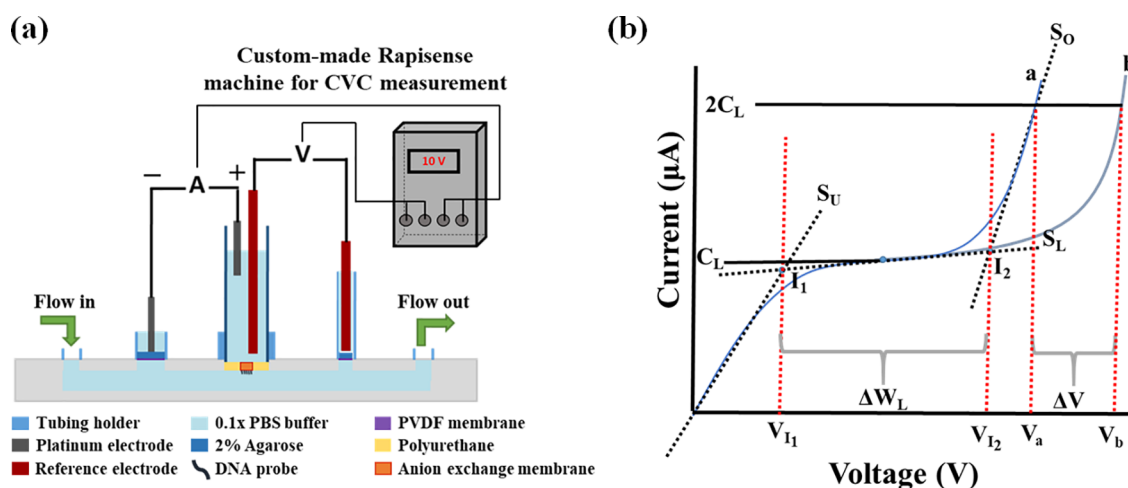

Figure 3. (a) Schematic diagram of the biosensing system and (b) definition of parameters in the CVC measurement.

was treated with EDC solution, prepared by adding 11.4 mg of *N*-(3-(dimethylamino)propyl)-*N*′-ethylcarbodiimide hydrochloride) in 150 μL of MES buffer, pH 5.5, for 45 min.[36] The EDC-modified membrane sensor head was incubated with 20 μL of 10 μM amine-ended DNA probe solution as previously described for overnight at 4 °C. Figure 2 shows the scheme of the two-step DNA probe functionalization reactions on the membrane surface. The obtained DNA probe functionalized AEM sensor head was stored in 0.1× PBS buffer, pH 7, before tests.

Biosensing System. The biosensing system contains four electrodes, an AEM sensor head, a microfluidic biochip, and Rapisense (a current−voltage measuring system, developed by Engineering and Design Core Facility at the University of Notre Dame). Two reference electrodes, made by Ag−AgCl, were used to determine electrical potential differences when two platinum electrodes applied the current within 0−100 μA at a scan rate of 1 μA/s. Before CVC curves were measured, the sensor and two reference reservoirs were filled with 0.1× PBS buffer, pH 7, and the AEM sensor head was inserted into the microfluidic channel. The arrangement of four electrodes is shown in Figure 3a. In each experiment, the first CVC curve was obtained after the microfluidic channel was washed by 4× PBS buffer, pH 7, for 15 s and 0.1× PBS buffer, pH 7, for 5 min. After the first curve was established, three repeated runs were performed to set the overlapped curves as the baseline. The sensor then was washed by 0.1× PBS buffer, pH 7, for 1 min among each run. The DNA sample (60 μL) was injected into the channel and incubated 15 min for hybridization between target DNA fragments and probes. Nonspecific DNA was removed by the same washing steps mentioned above until the CVC reaches a reproducible voltage shift. The transgenic soybean sample could be detected by the voltage shift in the over-limiting region (Figures 1 and 3b) due to the specific binding between sample DNAs and probes.

To observe current−voltage characteristic behavior, all parameters are defined as shown in Figure 3b,[37] where S_U, S_L, and S_O are the slopes (μA/V) of under-limiting, limiting, and over-limiting regions, respectively. I_1 is the intersection point of S_U and S_L, and I_2 is the intersection point of S_L and S_O. The limiting current (C_L) is obtained as the average of I_1 and I_2 to define the applied current in limiting region. The width of limiting current (ΔW_L) between $V_{(I1)}$ and $V_{(I2)}$ can be applied to estimate the resistance of the membrane. The critical parameter is the voltage shift (ΔV) from V_a to V_b at a current of twofold of the limiting current ($2C_L$). The voltage shift (ΔV) demonstrates the biosensing signal from the target DNA hybridization. A receiver operating characteristics (ROC) analysis method using easyROC software (ver. 1.3.1) was adopted to determine a cut-off value of the voltage shift for the negative and positive control samples of each sensor.[38] The negative and positive samples are correspondingly defined as 0 and 1 in the software, which delivers the cut-off point depending on how well it classifies the designated sample range.

Membrane Characterization. *Ion Exchange Capacity (IEC).* To define the fixed charge on the membranes, a back-titration technique was used to measure the IEC in the AEM.[39] A membrane weighing about 0.7 g was cleaned first, dried in an oven overnight, and then immersed in 100 mL of 1 M HCl$_{(aq)}$ solution for 24 h to fully saturate the quaternary amine in the membrane with chloride ion. Next, the membrane was washed by deionized water to remove excess HCl. After the pH reached a stable value, the membrane was soaked in 50 mL of 1 M Na$_2$SO$_{4(aq)}$ for 24 h. Sulfate ions would replace chloride ions in the membrane, and almost all chlorine ions were extracted into the solution. An indicator of 0.1 M K$_2$CrO$_4$ was added to the solution, and then the prepared solution was titrated against 0.1 M AgNO$_{3(aq)}$ until the solution turning color from white AgCl precipitate to orange brown to indicate the titration end point. The IEC in the AEM can be
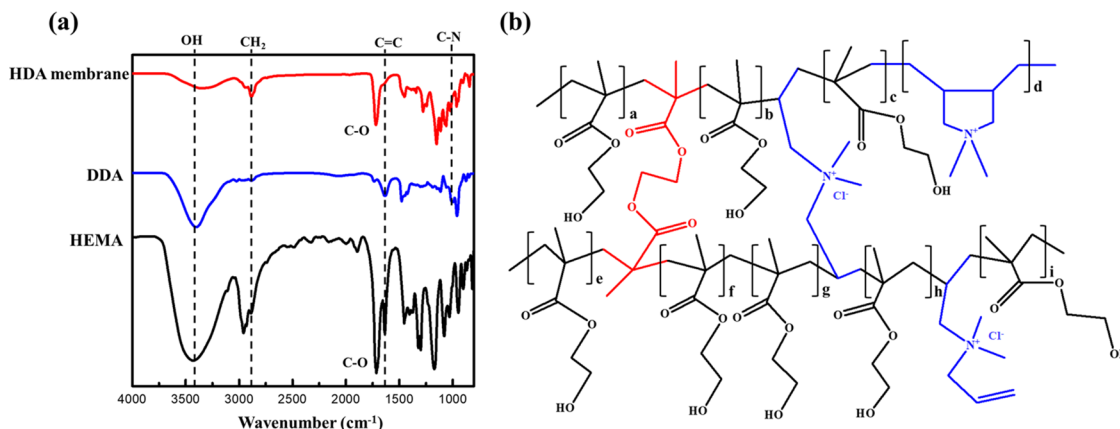
Figure 4. (a) Infrared spectra of HEMA and DDA monomers and HDA membranes. (b) Suggested chemical structure of the HDA membranes. The blue color indicates the DDA moieties that contribute the quaternary amine groups, the black color shows the HEMA units, and the red color represents the cross-linker EGDMA.
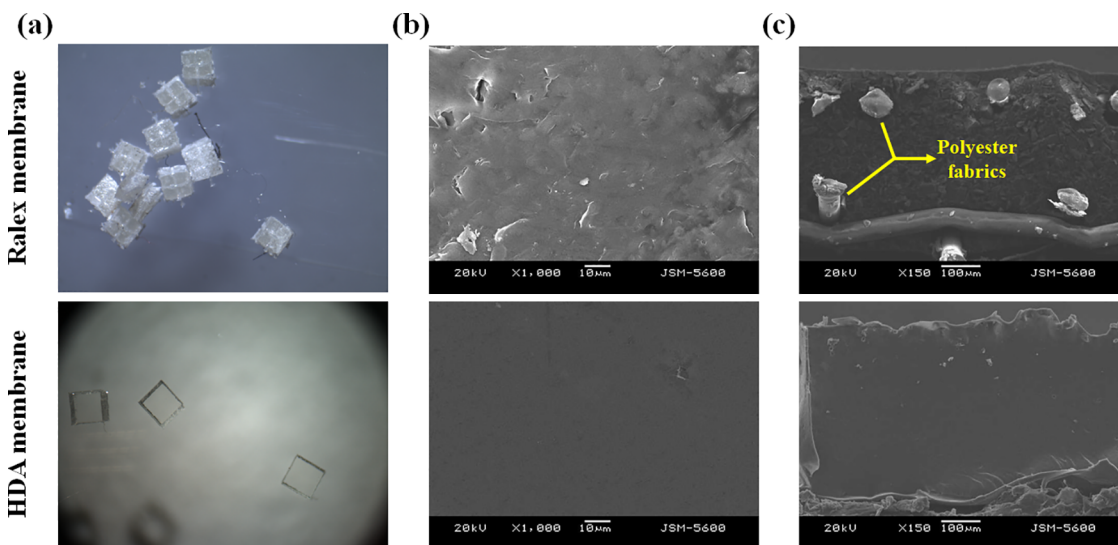
Figure 5. (a) Optical microscopic images (the size of each piece is 0.5×0.5 mm^2). (b) SEM surface morphology; scale bar: 10 μm. (c) SEM cross-sectional microstructures of commercial Ralex membrane (top panel) and synthesized HDA membrane (bottom panel); scale bar: 100 μm.

determined by substituting the volume of AgNO$_3$ used into the following equation:

$$\text{IEC} = \frac{\text{vol of AgNO}_3\,(\text{mL}) \times \text{concn of AgNO}_3 \left(\frac{\text{mmol}}{\text{mL}}\right)}{\text{wt of dry membrane (g)}} \quad (1)$$

Water Uptake and Degree of Swelling. The water uptake and degree of swelling were measured with equal size membranes ($L \times W \times H = 0.25 \times 0.25 \times 0.5$ mm^3). Both measurements were done while the weight and dimension reached equilibrium. These properties were calculated by the following equations:[40]

$$\text{water uptake (\%)} = \frac{W_W - W_D}{W_D} \quad (2)$$

where W_W is the weight of the wet membrane, saturated in deionized water for 24 h, and W_D is the weight of the dried membrane.

$$\text{degree of swelling (\%)} = \frac{L_f - L_i}{L_i} \quad (3)$$

where the L_f is the length of the wet membrane and L_i is the length of the dried membrane (L can be replaced by width and height).

Chemical Functional Group Analysis. Fourier transform infrared spectroscopy (PerkinElmer Spectrum 100) was used to confirm the characteristic chemical functional groups presented in the membranes. All spectra were recorded from 64 scans with a 4 cm^{-1} resolution at the range from 4000 to 650 cm^{-1}. Two kinds of Fourier transform infrared techniques including transmission and attenuated total reflection modes were applied to observe the functional groups of HEMA and DDA monomers and HDA membranes.

Optical and Scanning Electron Microscopy. The images of cut membranes were observed by using stereo microscope (Bestscope, BS-3000). To obtain the clear surface morphology and cross-sectional microstructures, all the membranes were dried in an oven overnight at 50 °C and then observed with the scanning electron microscope (SEM, JEOL JSM-5600) at an accelerating voltage of 20 kV.

Surface Chemical Composition Analysis. X-ray photoelectron spectroscopy (XPS) was applied for the measurement of the chemical composition on the membrane surface. Each element has a different specific electron binding energy in various functional groups, so the detection of photoelectron kinetic energy by XPS can identify elements and also the chemical bonding on the membrane surface. Before analysis, the samples were placed on a copper foil tape and dried in an oven overnight. XPS experiments were operated under an ultrahigh vacuum using the VG ESCALAB 250 X-ray photoelectron spectroscope (Thermo Fisher Scientific, UK) with the mono X-ray Al Kα at 1486 eV and 72 W power at the anode. The C1s spectrum around 284.5 eV was deconvoluted by using XPSPEAK4 software to
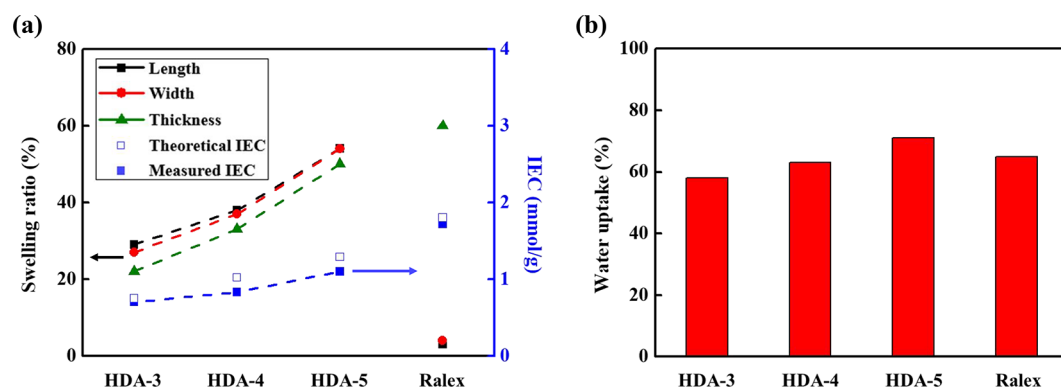
Figure 6. (a) Swelling ratio of dimensional change with correlation of measured and theoretically estimated IEC. (b) Water uptake of the synthesized HDA membranes and commercial Ralex membrane.

identify particular chemical bonds with the carbon element on the membrane surface.

RESULTS AND DISCUSSION

Synthesis of Homogeneous DDA-Based AEMs (HDA) Membranes. The HDA membranes were synthesized by photoinitiated free radical polymerization of HEMA and DDA as described above, and the chemical structure of the membranes was confirmed by FTIR spectra, shown in Figure 4a. All the spectra of chemicals contain a broadband at 3700–3300 cm^{-1} corresponding to hydroxyl (−OH) bond and peak at 2950–2850 cm^{-1} due to C−H stretching in the alkyl group. Compared to that in HEMA and DDA monomers, the peak of C=C stretching at 1625 cm^{-1} decreased significantly in the HDA membranes, indicating that a successful polymerization had occurred.[41] The UV curing process leads to polymerization by breaking the π bond of C=C in the monomers and forms the main chain of the polymer. However, a weak C=C stretching shoulder was observed in the HDA membranes because of the incomplete reaction of the divinyl groups in DDA during UV treatment. The stretching at 1040 cm^{-1} indicated that the HDA membranes contain quaternary amine from DDA monomer.[42] Based on the FTIR spectrum data, HDA membranes was synthesized successfully, and a suggested chemical structure of the membrane is illustrated in Figure 4b. The DDA moieties contributed to the quaternary amine and presented in the main chain of the polymer membranes synthesized here. Furthermore, they might function as cross-linkers or remain unreacted vinyl ends in the membranes.[43]

Optical microscopy and SEM were applied to make micromorphological observation of the membranes. The commercial Ralex membrane is composed of anion exchange resin particles and two layers of fibrous support, as shown in Figure 5a−c of the top panel. Support fibers were easily identified in the optical micrograph (Figure 5a) and the cross-sectional SEM image (Figure 5c). The heterogeneous structure was clearly observed with structural irregularities on the membrane surface and its cross section. These structural irregularities may cause the inconsistency in DNA probe functionalization and the CVC measurement. The synthesized HDA membranes exhibited homogeneous structure as a smooth membrane surface, and no fibers were observed in cross section, as shown at the bottom panel of Figure 5a−c. It expected that the homogeneous structure would lead to a better performance in our membrane biosensing system.

Swelling and Ion Exchange Capacity of Unmodified AEMs. The formulation of the membrane materials is a crucial part of the fabrication of anion-exchange membranes. To promote the binding efficiency between the membrane sensor and target DNA, a higher IEC content AEM might be preferred. However, the HDA membranes with a high fixed charge content (DDA/HEMA = 6/10) could not be embedded well into the sensor head because of a high degree of swelling. As a result, the membranes with DDA/HEMA = 6/10 were screened out in the experiment. Only three kinds of membranes (HDA-3, HDA-4, and HDA-5) with various DDA/HEMA ratios (3/10, 4/10, and 5/10, respectively) were further characterized, and their swelling properties (swelling ratio and water uptake) and ion exchange capacity (IEC) in comparison with that of the commercial membrane are presented in Figure 6. The swelling ratio of HDA-3 membranes is around 20−30%, that of HDA-4 membranes is around 30−35%, and that of HDA-5 membrane is around 50%. Moreover, the measured and theoretically estimated IEC values were quite close, which also confirmed the success of membrane synthesis. The stronger fixed charge in the membrane caused significant osmotic pressure difference; therefore, water would be absorbed from the external solution to the inner side of the membrane to balance the difference. The IEC of HDA membranes are in the range from 0.65 to 1.2 mmol/g, and the commercial one is around 1.6 mmol/g. The higher quaternary amine content and IEC in the membrane would lead to a higher swelling ratio (Figure 6a). Compared with the commercial membrane, the dimensional changes of the HDA membrane are nearly isotropic due to the homogeneous structure. On the contrary, the fiber support of the Ralex membrane restricts the swelling in x- and y-directions (<5%) and a significant increase in thickness (60%). The water uptake data further demonstrated a similar trend (Figure 6b). Both IEC and water uptake of HDA membranes would increase with the quaternary amine content. Because of the hydrophobic nature of its binder and support, the Ralex membrane can maintain a quite high IEC but a moderate water uptake (65%). On the other hand, the HDA membranes show a relatively lower IEC at similar water uptake levels (62−72%). To keep a relatively stable membrane dimension, the DDA content must be kept below 60% of HEMA in the synthesized HDA membranes.

Current−Voltage Characteristic (CVC) Behaviors of Bare AEMs. Typical current−voltage characteristic (CVC) curves of various HDA and Ralex AEMs without any surface
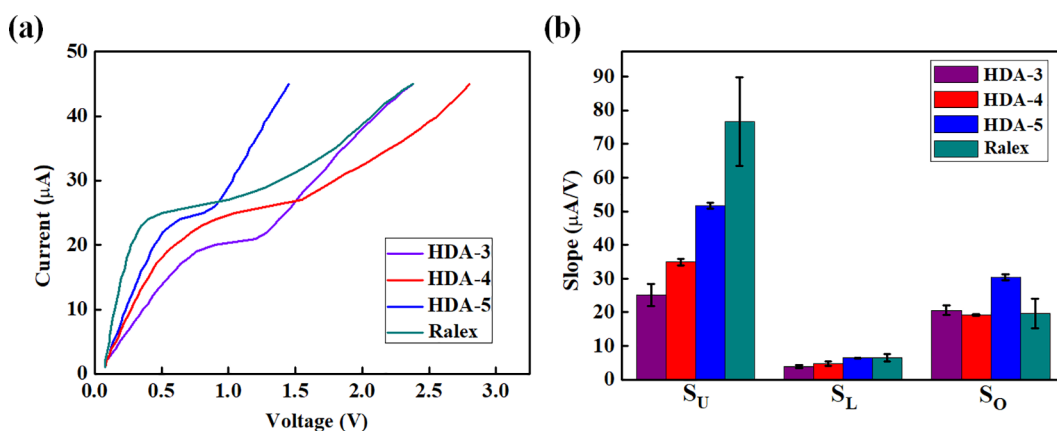
Figure 7. (a) CVC curves and (b) slope values of three regions in the CVC curves of various bare AEMs. S_U = the slope of an under-limiting region, S_L = the slope of a limiting region, and S_O = the slope of an over-limiting region. The bar indicates the standard deviation from three measurements.

modification are shown in Figure 7a. All of them showed a characteristic under-limiting region, a limiting region, and an over-limiting region generally observed in an ion exchange membrane under current–voltage scan due to the phenomenon of concentration polarization.[44] The HDA-2 (DDA/HEMA = 2/10) membrane could not produce a smooth CVC curve within the voltage range (data not shown). It seemed that a minimum IEC in the AEM was required to generate the limiting current behavior. Therefore, the performance of membranes with DDA/HEMA = 2/10 or lower DDA content was not discussed in this report. The CVC curves of the rest of the AEMs were analyzed to obtain the slope in each region according to the method presented previously in Figure 3b. Every membrane was tested in three replicates, and each was cut from the same piece of AEM of the same size. The results of slope in each region (S_U, S_L, and S_O) indicated that the HDA membranes possessed much lower standard deviation (error bar) than the Ralex membrane (Figure 7b). The matrixed fibrous support of the Ralex membrane might create erratic resistance in each membrane, leading to a considerable slope variation. In contrast to the heterogeneous Ralex membrane, the homogeneous structure of HDA membranes showed a much lower variation and better reproducibility in the CVC measurement.

It would be of interest to discuss the quantitative effect of IEC on the CVC slope in each region. The under-limiting region represents the Ohmic behavior of the membranes. Higher IEC in the AEMs would provide better ion conductivity and lower the ion transport resistance; therefore, S_U increased with the IEC of the membrane (HDA-3 < HDA-4 < HDA-5 < Ralex membrane) in the CVC measurement. As the applied voltage through the AEMs increases, the concentration of the electrolytes on the cathode side membrane surface decreases (depletion or desalting side); meanwhile, the concentration of the electrolytes on the other (anode) membrane surface increases (concentration side). This phenomenon is also known as the concentration polarization in membrane electrodialysis. Within the boundary layer, anions are not only driven by the electrical field but also attracted by the opposite charge in the AEMs. Therefore, anions would transport faster because of intense fixed positive charges on the membrane surface, leading to short supply or depletion of anions within the boundary layer.[45,46] The anion transport dropped significantly due to the depletion to produce

the limiting-current regime with a near-infinity differential resistance. Because of this phenomenon, the slope of the limiting region (S_L) was small and very much similar but still showed an order of Ralex membrane > HDA-5 > HDA-4 > HDA-3 according to the order of IEC in the AEMs. Further increasing the voltage, the electroconvective instability set in and produced microvortices around the boundary layer near the membrane surface.[47,48] Ideally, the microvortices would bring in ions to refill the depletion zone and return the system to Ohmic differential resistance in the under-limiting region, albeit with a shift due to the limiting-current interval. However, all the AEMs showed a lower slope in the over-limiting region (S_O) than that in the under-limiting region (S_U) due to higher total transmembrane resistance. This suggests that the vortex mixing is not complete, and there remain ion-depleted regions that increase the resistance. Except HDA-5, three other membranes (HDA-3, HDA-4, and Ralex membranes) showed very similar values in the slope of the over-limiting region (S_O). This observation suggests that the overall membrane resistance (ion flux) is sensitively controlled by the microvortex geometric structure and intensity on the membrane surface, which are in turn affected by the membrane curvature.

Earlier experimental studies[22,49−51] did suggest this strong sensitivity of the microvortices on the surface curvature. In addition, theoretical studies by Chang et al. also suggested that a Dukhin type curvature-induced polarization can produce intensified vortices of specific size related to the curvature, in contrast to the randomly sized vortices produced by electro-osmotic instability.[52,53] The Slouka group visualized the dynamic patterns of microvortices through fluorescently labeled melamine resin microparticles to confirm that the flat or convex geometry of the ion exchange membrane surface would affect the slope of the over-limiting region due to the discrepancy of the patterns of microvortices. As CVC reached the over-limiting range, an array of small microvortices formed on the convex surface, and they could thoroughly destroy the depletion zone by intense mixing. For the flat membrane surface, a counter-rotating inflow formed from the membrane edge, and the shear force by the resulting outflow from the membrane center pushed the ion-depleted region further back into the bulk to produce a large mushroom-like depletion zone at the beginning of the over-limiting range, as shown in Figure 8. This edge effect is most likely due to the high fields at the corners of the conducting membrane and is usually not
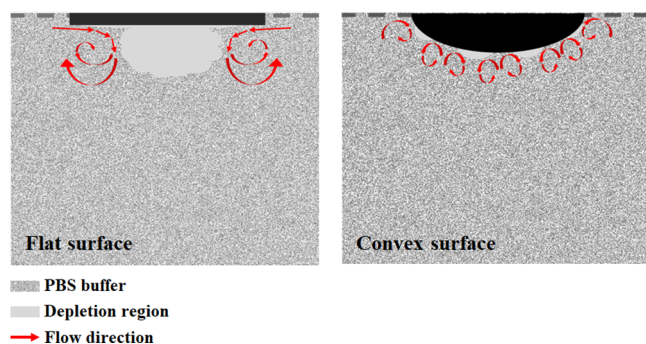
Figure 8. Schematic mechanism of microvortices at different surface curvatures on top of a 500 μm membrane (illustrative drawing sketched according to refs 22 and 49−51).

with DNA probes did not show a complete CVC curve within 10 V (Figure 10), and this may due to its low positively

Figure 10. Current−voltage characteristic curves of HDA-3, HDA-4, and HDA-5 membranes after DNA probe functionalization.

considered in the classical electroconvection instability theory. It enlarges the ion depletion region on the membrane and increases the cross-membrane resistance. It also reduces the efficiency of the subsequent electro-osmotic vortices in bringing ions to the depleted region. As a result, the membrane with a convex surface and a smoother edge should have a lower transmembrane resistance and a higher slope in the over-limiting region.
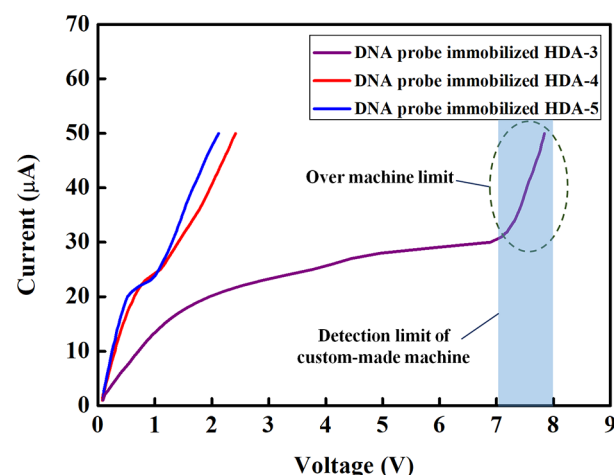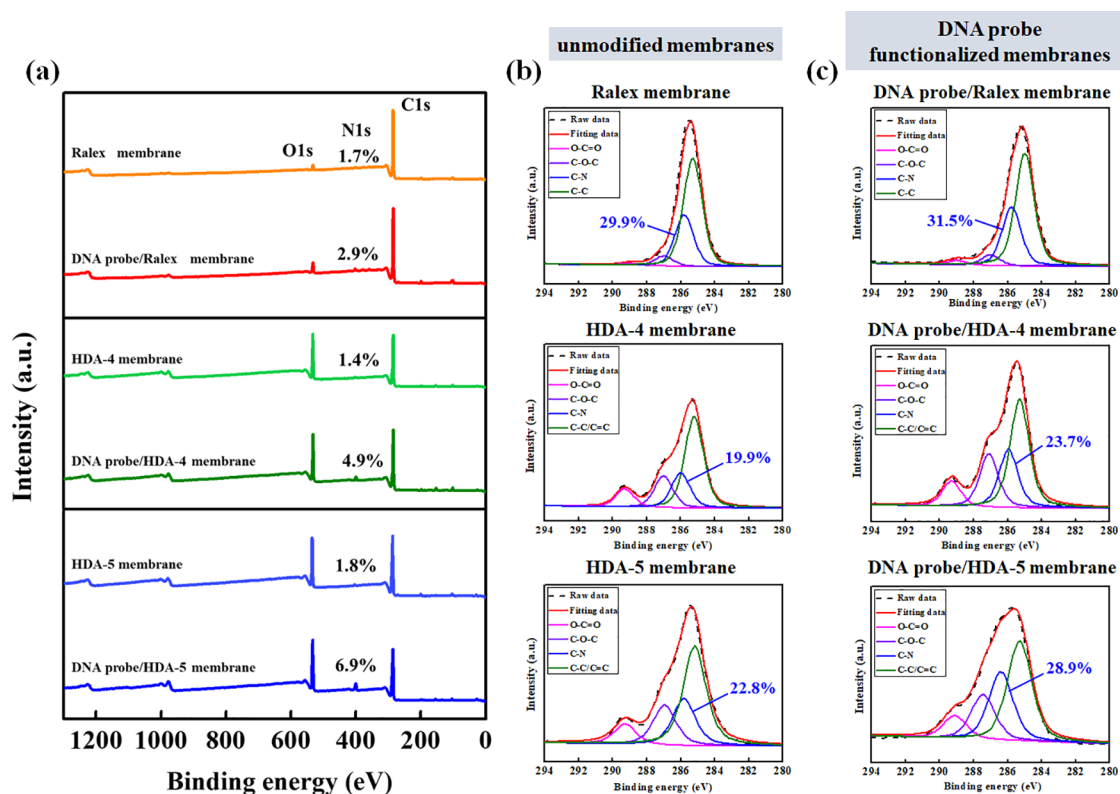
It was speculated that the CVC curves of the synthesized membrane are also affected by the patterns of the micro-vortices formed near the membrane surface. To confirm the effect, the side view of those membrane sensor heads under optical microscopy was observed and shown in Figure 9. It was found that HDA-3, HDA-4, and Ralex membranes were embedded well in the sensor head and a flat membrane surface was preserved, but the HDA-5 membrane swelled out because of the higher swelling ratio (>50%) shown above, and a convex membrane surface was clearly identified. It was possible that the convex HDA-5 membrane could generate many small swirling eddies or microvortices near the membrane surface in the over-limiting region so that the electrolyte could migrate into the membrane surface faster and result in a higher over-limiting slope than other membranes as shown in Figure 7b. The patterns of microvortices might also affect the voltage shift after DNA hybridization in the over-limiting range, as will be discussed in the next section.

DNA Probe Functionalized AEMs. An explicit current−voltage characteristic behavior could be observed in the bare HDA-3, HDA-4, and HDA-5 membranes as presented above. However, the anion exchange membranes are required to attach DNA probe for specific binding with target genes. When the negatively charged DNA probe was functionalized onto the membrane, it created a charge inversion on the membrane surface. The CVC curves of the HDA-3 membrane attached
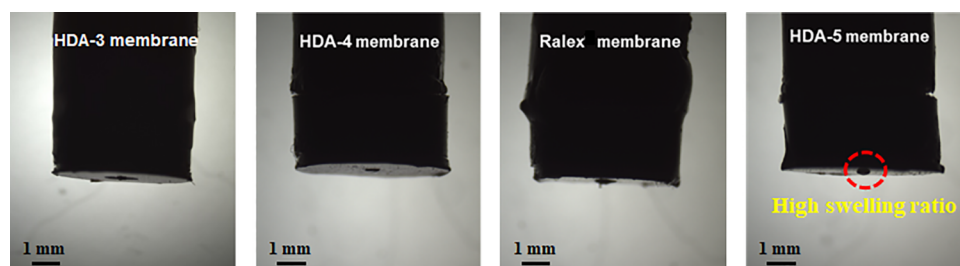
charged ion exchange capacity. The result suggests that a minimum IEC is needed in the membrane formulation to obtain a suitable limiting current behavior in the CVC measurement for DNA detection. On the other hand, the DNA probe functionalized HDA-4 and HDA-5 membranes both showed adequate CVC curves; therefore, they would have the potential for specific DNA binding application. According to these results, the DDA/HEMA ratio of HDA membranes should be limited with a range between 4/10 and 5/10, and the HDA-3 membrane was screened out from further tests.

DNA probe functionalization would change the surface chemistry of the membranes; therefore, the XPS technique was applied to reveal the change of surface chemical information before and after DNA probe functionalization. The XPS spectra of unmodified and DNA probe functionalized HDA-4, HDA-5, and Ralex membranes are shown in Figure 11. The XPS survey spectrum showed the sharp peaks at 540 eV (O1s), 410 eV (N1s), and 295 eV (C1s) to indicate the signature chemical elements of oxygen, nitrogen, and carbon on the membrane surface, respectively. Because of the presence of an abundant amount of nitrogen in DNA molecules, the successful functionalization of DNA probes on various AEMs made increased the intensity of the N1s peak,[54] as shown in Figure 11a. In addition, N1s peaks were enhanced by fixed charge quaternary amine in the HDA membranes. The bare HDA-5 membrane showed a higher N1s content (1.8%) than the bare HDA-4 membrane (1.4%). Interestingly, the Ralex membrane showed a slightly lower N1s content (1.7%) than

Figure 9. Side view of various membrane sensor heads under optical microscopy (membrane size: 0.5 × 0.5 mm^2).

Figure 11. XPS survey spectra and the high-resolution C1s spectra of unmodified and DNA probe functionalized HDA-4, HDA-5, and Ralex membranes. (a) Full scan spectra of all the membranes, (b) C1s spectra of unmodified membranes, and (c) C1s spectra of DNA probe functionalized membranes.

the HDA-5 membrane although the Ralex membrane had the highest quaternary amine content (or IEC) among all tested AEMs probably because the inhomogeneity of the membrane may cover some quaternary amine on the membrane surface. Furthermore, the increment of N1s content after DNA immobilization on both HDA membranes (more than 3.5-fold increase) was much more pronounced than that of the Ralex membrane (1.7-fold), indicating the synthesized HDA membranes might have better functionalization efficiency following the same DNA probe modification protocol.

To characterize the chemical bonds of the functionalized DNA probes, the high-resolution C1s spectra were deconvoluted into several peaks. These deconvoluted peaks included C−C/C═C with a binding energy of 285 eV, C−N with a binding energy of 286 eV, C−O−C with a binding energy of 287 eV, and O−C═O with a binding energy of 289 eV; also the chemical bond composition of unmodified and DNA probe immobilized membranes are shown in Figures 11b and 11c, respectively. The exact numbers are tabulated in Table S1. The C−C is the primary chemical bond of polymer; therefore, the highest intensities were observed on all the unmodified and probe modified membranes. On the other hand, the O−C═O and C−O−C bonds were detectable on both HDA and Ralex membranes. Because of the methacrylate moieties of HEMA and EGDMA in the main structure of HDA membranes, the observed intensities of these two chemical bonds of HDA membranes were much stronger than that of the commercial Ralex one. Moreover, the increasing ratio of the C−N bond after probe immobilization was attributed to the DNA probe attachment.[55,56] It can be identified that the increment of C−N bond was also more significant on both HDA membranes

(4.8% in HDA-4 and 6.1% in HDA-5) than the Ralex membrane (1.8%). It further confirmed that the synthesized HDA membranes have much better functionalization efficiency of DNA probes than the commercial membrane.

The two-step DNA functionalization protocol in this study includes carboxylation of the AEMs with 3,3,4,4-benzophenonetetracarboxylic acid and then the EDC coupling of amine-end DNA probe as shown in Figure 2. The carboxylation step might have proceeded better on HDA membranes than the Ralex membrane because the UV grafting happened not only by the hydrogen abstraction from the membrane surface but also on the residual vinyl groups of DDA in the HDA membranes.[48] The higher carboxylation efficiency would leave more reactive sites for later EDC coupling; therefore, the synthesized HDA-4 and HDA-5 membranes had better DNA immobilization efficiency than the commercial one. Moreover, the HDA-5 membrane has higher fixed positive charge content than the HDA-4 membrane. The higher fixed positive charge content might be able to attract more partially negatively charged 3,3,4,4-benzophenonetetracarboxylic acid at pH 7[49] close to the membrane surface for the UV photografting reaction of carboxylation. Therefore, the HDA-5 membrane performed a better DNA functionalization efficiency than the HDA-4 membrane. Because of DNA probe functionalization, the increment of both the N1s and C−N peak intensities in the spectra showed that HDA-5 > HDA-4 > Ralex membrane, indicating a significantly higher probe density on the surface.

Detection of GM Soybean Target Genes Using AEMs Sensors. The DNA probe immobilized HDA-4, HDA-5, and Ralex membrane sensors were tested in the microfluidic
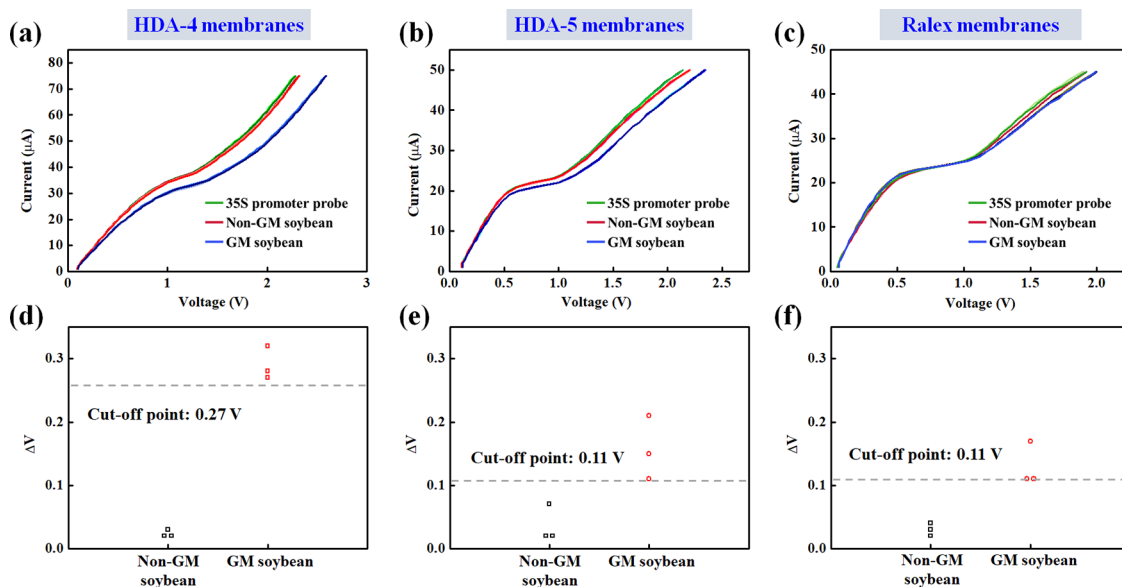
Figure 12. Resulting characteristic curves and scatter plots of (a, d) HDA-4, (b, e) HDA-5, and (c, f) Ralex membranes in the specific binding test for GM soybean identification.
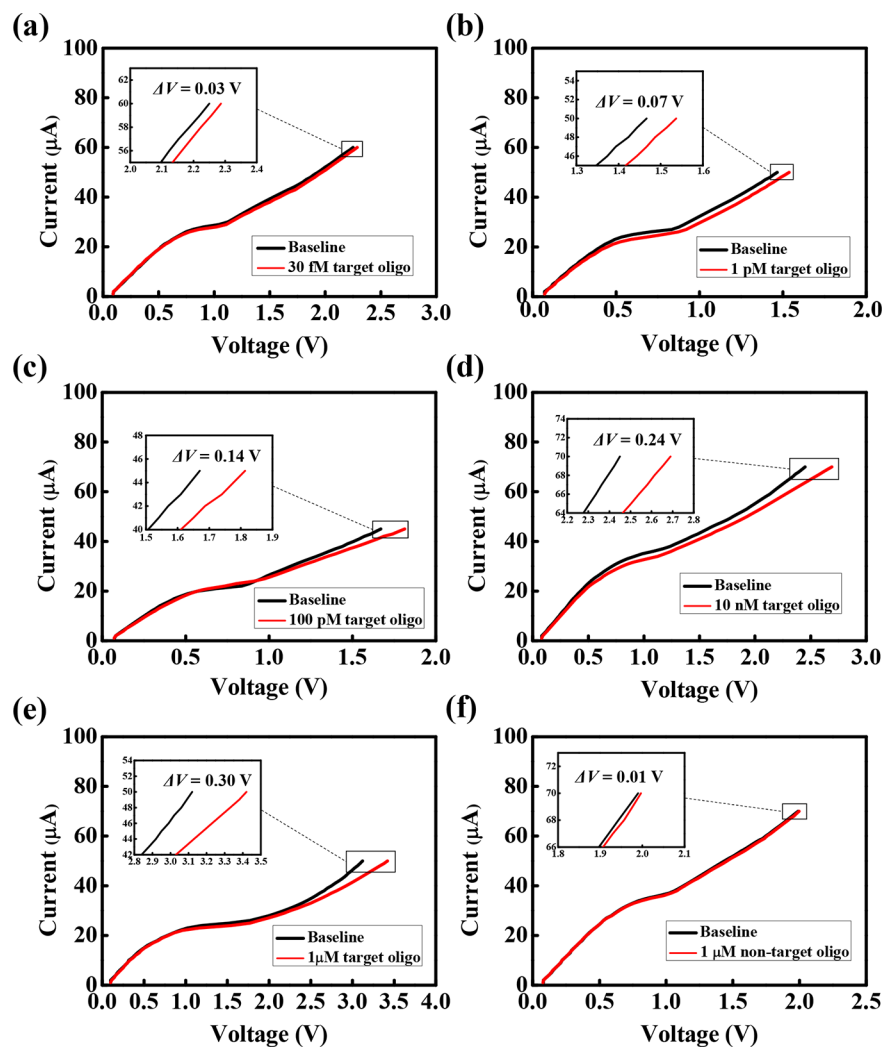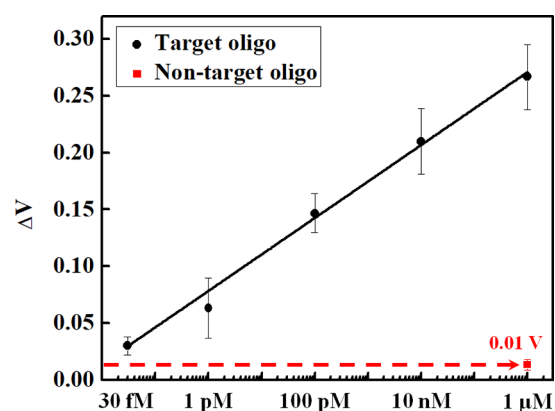

Figure 13. Voltage shift blow-up of target gene oligo in a range from 30 fM to 1 μM with the HDA-4 membrane sensor in the CVC measurements and the blow-up with 1 μM nontarget gene oligo.

biochip of the biosensing system for the recombinant virus 35S promoter DNA target in genetically modified soybean (GM soybean). The PCR amplified DNA samples were injected into the biochip to hybridize the target gene with the probe by incubation for 15 min. Nonspecific binding substances were washed by PBS solution. The CVC measurement was performed for these samples with three repeats. The CVC curves of HDA-4, HDA-5, and Ralex membrane sensors to detect are shown in Figures 12a, 12b, and 12c, respectively. The voltage shift (ΔV) of each sensor for the non-GM and GM soybean samples is shown in Figures 12d, 12e, and 12f. The distinct difference in the voltage shift could be identified for the wild-type non-GM and GM soybean samples in all sensors. A receiver operating characteristic (ROC) analysis method was adopted to determine the cut-off value for the diagnostic test of negative and positive samples for each sensor.[38] The cut-off point of Ralex, HDA-4, and HDA-5 membrane sensors was 0.11, 0.27, and 0.11 V, respectively. The HDA-4 membrane sensor showed the highest voltage shift and cut-off point to the positive samples, which was much better than that of the Ralex and HDA-5 membrane sensors. The higher numbers of immobilized DNA molecules on the HDA-4 membrane sensor might account for the more sensitive change of the voltage shift. However, the HDA-5 membrane sensor with even more DNA probes immobilized on the surface showed an unexpected lower voltage shift than the HDA-4 membrane sensor. The formation of many small microvortices near the convex membrane surface might also account for the smaller voltage shift than that on the flat membrane, as demonstrated in the studies by Slouka's group.[49−51] The membrane sensors with the flat surface were more sensitive to target DNA attachment and presented a significant voltage shift. The same effect also happened in our experimental results so that the HDA-4 membrane sensor showed a higher voltage shift than the HDA-5 membrane sensor (Figure 12d,e). In summary, HDA-4 is the most appropriate membrane formulation for GM soybean identification. The data in Figure 12a are taken for three different sensors, and they exhibit a variation of no more than 7.5%, validating the cross-sensor reproducibility of the HDA-4 synthesis method.

Reproducibility, Dynamic Range, and Detection Limit of the HDA-4 Membrane Sensor. The sensitivity test for the HDA-4 membrane sensor in the microfluidic biochip of the biosensing system was performed with various concentrations of model target oligo for CVC measurement. The stock solution was diluted with 0.1× PBS to a range from 30 fM to 1 μM; then, the sensor was incubated with an oligo sample of predetermined concentration following the same procedures described for a standard CVC measurement. All the samples were tested with three replicates. The resulting CVC with voltage shift blow-up, average voltage shifts, and their standard deviations stemming from target DNA hybridization are shown in Figures 13 and 14. Each frame in the figure is measured with a different sensor. Although the limiting current show about a 30% variation due to sensor head manufacturing inconsistencies, the voltage shift collapsed into a universal calibration curve in Figure 14, indicating the reproducibility of our sensors.

The voltage shift was proportional to a logarithm scale oligo concentration with an acceptable standard deviation of the range from 30 fM to 1 μM. The corresponding regression equation can be expressed by $\Delta V = 0.271 + 0.032 \log C$ (C:

Figure 14. Voltage shift (dark circle) vs logarithm scale concentration of target gene oligo, ranging from 30 fM to 1 μM, with the HDA-4 membrane sensor in the CVC measurements using the microfluidic biochip and the voltage shift (red square) of the test with a 1 μM nontarget gene oligo (n = 3 experiments). The red dashed line indicates the noise level.

μM, $R^2 = 0.995$). The voltage shift was not linearly correlated to the target DNA concentration because of the complexity of how the screened field of the charged membrane nucleic acids affects the electroosmotic microvortex formation and intensity. The shift has a logarithm dependence on the DNA concentration, as is consistent with earlier reports.[14,25] This weak dependence accounts for the large dynamic range, which could be advantageous for unknown sample screening analysis. Besides, the voltage shift from 1 μM nontarget oligo (no matched sequence to the DNA probe) detection was only about 0.01 V. This voltage shift due to a possible nonspecific binding of the nontarget gene at a very high concentration could be considered as the noise during CVC measurement for specific detection of the target gene. According to the detection limit guideline,[59] a meaningful measurement requires a minimum signal-to-noise ratio of 3. Notably, a 0.03 ± 0.01 V shift was obtained when the HDA-4 membrane sensor was incubated with a 30 fM target oligo sample. The voltage shift at 30 fM oligo was about 3 times of the noise; thus, it can be considered as the detection limit of the sensor with the well-prepared target oligo. Compared to the results reported for the Ralex membranes,[14] this study extended the lower detection limit down to 30 fM and provided a wide dynamic detection range of nearly 8 decades for the oligo gene detection. This 30 fM detection limit represents the best reported in the literature by 2 orders of magnitude, corresponding to about 10000 copies with our sample volume. Because of the reduced surface heterogeneity, noise is suppressed at low copy numbers and higher density probe functionalization can be achieved. Both effects improved the detection limit and the dynamic range by 2 orders of magnitude, without sacrificing selectivity. The results demonstrate that the self-synthesized homogeneous HDA-4 membrane is suitable for the reproducible and sensitive nucleic acid detection via current−voltage characteristic measurement with the use of the proposed microfluidic biosensing platform.

■ CONCLUSIONS

In this work, we demonstrated the preparation, characterization, probe functionalization, and validation of hydrogel-based AEMs for transgenic soybean identification by voltage shift stemming from the target DNA hybridization on the

membrane surface. These newly synthesized AEMs not only provided a homogeneous structure for reproducible performance and high-density probe functionalization but also enhanced the sensitivity of the sensor. The tunable formulation of HDA membranes allowed the study of the effect of ion exchange capacity on the current–voltage characteristic curves and specific target gene identification. It was found that the HDA-4 (DDA/HEMA = 4/10) membrane gave the best overall performance on the detection of recombinant 35S promoter target sequence commonly existed in commercial GM soybean. The results also demonstrated that membrane surface geometry would be a determining factor for the voltage shifting in the over-limiting region because the electroconvective microvortices that opposes ion depletion were highly sensitive to the membrane curvature, which we optimized by controlling the swelling. The self-synthesized HDA-4 membrane outperformed the previously used commercial Ralex membrane with a much better detection limit for identification of GM soybean recombinant gene. Furthermore, the one-pot photoinitiated polymerization technique for AEM preparation can be applied for the *in situ* integrated membrane sensor head fabrication in the future, instead of the membrane cutting and embedding method used currently. The newly developed membrane synthesis method will hence significantly advance the scope of application of this novel nucleic acid sensing technology.

ASSOCIATED CONTENT

ⓢ Supporting Information

The Supporting Information is available free of charge at https://pubs.acs.org/doi/10.1021/acsami.0c17180.

Figure S1 and Table S1 (PDF)

AUTHOR INFORMATION

Corresponding Author

Yi-Ming Sun − *Department of Chemical Engineering and Materials Science and Graduate School of Biotechnology and Bioengineering, Yuan Ze University, Taoyuan, Taiwan 32003, Republic of China; R&D Center for Membrane Technology, Chung Yuan University, Taoyuan, Taiwan 32023, Republic of China;* ⓞ orcid.org/0000-0002-7779-8714; Phone: +886 3 4638800; Email: cesunym@saturn.yzu.edu.tw; Fax: +886 3 4559373

Authors

Jie-Ning Chuang − *Department of Chemical Engineering and Materials Science, Yuan Ze University, Taoyuan, Taiwan 32003, Republic of China*

Pei-Yin Diao − *Department of Chemical Engineering and Materials Science, Yuan Ze University, Taoyuan, Taiwan 32003, Republic of China*

Wen-Shan Huang − *Graduate School of Biotechnology and Bioengineering, Yuan Ze University, Taoyuan, Taiwan 32003, Republic of China*

Li-Fen Huang − *Graduate School of Biotechnology and Bioengineering, Yuan Ze University, Taoyuan, Taiwan 32003, Republic of China*

Satyajyoti Senapati − *Department of Chemical and Biomolecular Engineering, University of Notre Dame, Notre Dame, Indiana 46556, United States*

Hsueh-Chia Chang − *Department of Chemical and Biomolecular Engineering, University of Notre Dame, Notre Dame, Indiana 46556, United States*

Complete contact information is available at:
https://pubs.acs.org/10.1021/acsami.0c17180

Notes

The authors declare no competing financial interest.

ACKNOWLEDGMENTS

REFERENCES

(1) Roth, W. K. History and Future of Nucleic Acid Amplification Technology Blood Donor Testing. *Transfus. Med. Hemother.* **2019**, *46* (2), 67−75.

(2) Palchetti, I.; Mascini, M. Nucleic Acid Biosensors for Environmental Pollution Monitoring. *Analyst* **2008**, *133* (7), 846−854.

(3) Dooley, J. S. G. Nucleic Acid Probes for the Food Industry. *Biotechnol. Adv.* **1994**, *12* (4), 669−677.

(4) Marky, L. A.; Kupke, D. W. Enthalpy-Entropy Compensations in Nucleic Acids: Contribution of Electrostriction and Structural Hydration. In *Methods in Enzymology*; Elsevier: 2000; Vol. 323, pp 419−441.

(5) Nakano, S.-I.; Sugimoto, N. The Structural Stability and Catalytic Activity of DNA and RNA Oligonucleotides in the Presence of Organic Solvents. *Biophys. Rev.* **2016**, *8* (1), 11−23.

(6) Corless, C. E.; Guiver, M.; Borrow, R.; Edwards-Jones, V.; Kaczmarski, E. B.; Fox, A. J. Contamination and Sensitivity Issues with a Real-Time Universal 16S rRNA PCR. *J. Clin. Microbiol.* **2000**, *38* (5), 1747−1752.

(7) Scognamiglio, V.; Arduini, F.; Palleschi, G.; Rea, G. Biosensing Technology for Sustainable Food Safety. *TrAC, Trends Anal. Chem.* **2014**, *62*, 1−10.

(8) Leatherbarrow, R. J.; Edwards, P. R. Analysis of Molecular Recognition Using Optical Biosensors. *Curr. Opin. Chem. Biol.* **1999**, *3* (5), 544−547.

(9) Zhao, Q.-C.; Liu, M.-H.; Zhang, X.-W.; Lin, C.-Y.; Zhang, Q.; Shen, Z.-C. Generation of Insect-Resistant and Glyphosate-Tolerant Rice by Introduction of a T-DNA Containing Two Bt Insecticidal Genes and an EPSPS Gene. *J. Zhejiang Univ., Sci., B* **2015**, *16* (10), 824−831.

(10) Raymond, P.; Gendron, L.; Khalf, M.; Paul, S.; Dibley, K. L.; Bhat, S.; Xie, V. R. D.; Partis, L.; Moreau, M.-E.; Dollard, C.; Coté, M.-J.; Laberge, S.; Emslie, K. R. Detection and Identification of Multiple Genetically Modified Events Using DNA Insert Fingerprinting. *Anal. Bioanal. Chem.* **2010**, *396* (6), 2091−2102.

(11) Qiu, B.; Lin, Y.-B.; Lu, Y.-J.; Lin, Z.-Y.; Wong, K.-Y.; Chen, G.-N. Bioelectronics, A Novel Fluorescent Biosensor for Detection of Target DNA Fragment from the Transgene Cauliflower Mosaic Virus 35S Promoter. *Biosens. Bioelectron.* **2013**, *41*, 168−171.

(12) Fortunati, S.; Rozzi, A.; Curti, F.; Giannetto, M.; Corradini, R.; Careri, M. Novel Amperometric Genosensor Based on Peptide Nucleic Acid (PNA) Probes Immobilized on Carbon Nanotubes-Screen Printed Electrodes for the Determination of Trace Levels of Non-Amplified DNA in Genetically Modified (GM) Soy. *Biosens. Bioelectron.* **2019**, *129*, 7−14.

(13) Sun, W.; Zhong, J.; Qin, P.; Jiao, K. Electrochemical Biosensor for the Detection of Cauliflower Mosaic Virus 35S Gene Sequences Using Lead Sulfide Nanoparticles as Oligonucleotide Labels. *Anal. Biochem.* **2008**, *377* (2), 115−119.

(14) Senapati, S.; Slouka, Z.; Shah, S. S.; Behura, S. K.; Shi, Z.; Stack, M. S.; Severson, D. W.; Chang, H.-C. An Ion-Exchange Nanomembrane Sensor for Detection of Nucleic Acids Using a Surface

Charge Inversion Phenomenon. *Biosens. Bioelectron.* **2014**, *60*, 92−100.

(15) Egatz-Gomez, A.; Wang, C.; Klacsmann, F.; Pan, Z.; Marczak, S.; Wang, Y.; Sun, G.; Senapati, S.; Chang, H.-C. Future Microfluidic and Nanofluidic Modular Platforms for Nucleic Acid Liquid Biopsy in Precision Medicine. *Biomicrofluidics* **2016**, *10* (3), 032902.

(16) Jin, X.; Joseph, S.; Gatimu, E. N.; Bohn, P. W.; Aluru, N. R. Induced Electrokinetic Transport in Micro- Nanofluidic Interconnect Devices. *Langmuir* **2007**, *23* (26), 13209−13222.

(17) Mani, A.; Zangle, T. A.; Santiago, J. G. On the Propagation of Concentration Polarization from Microchannel- Nanochannel Interfaces Part I: Analytical Model and Characteristic Analysis. *Langmuir* **2009**, *25* (6), 3898−3908.

(18) Nandigana, V. V.; Aluru, N. R. Understanding Anomalous Current−Voltage Characteristics in Microchannel−Nanochannel Interconnect Devices. *J. Colloid Interface Sci.* **2012**, *384* (1), 162−171.

(19) Lee, H.-J.; Hong, M.-K.; Han, S.-D.; Moon, S.-H. Influence of the Heterogeneous Structure on the Electrochemical Properties of Anion Exchange Membranes. *J. Membr. Sci.* **2008**, *320* (1-2), 549−555.

(20) Belloň, T.; Polezhaev, P.; Vobecká, L.; Slouka, Z. Fouling of a Heterogeneous Anion-Exchange Membrane and Single Anion-Exchange Resin Particle by ssDNA Manifests Differently. *J. Membr. Sci.* **2019**, *572*, 619−631.

(21) Chang, H.-C.; Yossifon, G.; Demekhin, E. A. Nanoscale Electrokinetics and Microvortices: How Microhydrodynamics Affects Nanofluidic Ion Flux. *Annu. Rev. Fluid Mech.* **2012**, *44*, 401−426.

(22) Slouka, Z.; Senapati, S.; Yan, Y.; Chang, H.-C. Charge Inversion, Water Splitting, and Vortex Suppression Due to DNA Sorption on Ion-Selective Membranes and Their Ion-Current Signatures. *Langmuir* **2013**, *29* (26), 8275−8283.

(23) Cheng, I.-F.; Senapati, S.; Cheng, X.; Basuray, S.; Chang, H.-C.; Chang, H.-C. A Rapid Field-Use Assay for Mismatch Number and Location of Hybridized DNAs. *Lab Chip* **2010**, *10* (7), 828−831.

(24) Marczak, S.; Smith, E.; Senapati, S.; Chang, H. C. Selectivity Enhancements in Gel-Based DNA-Nanoparticle Assays by Membrane-Induced Isotachophoresis: Thermodynamics Versus Kinetics. *Electrophoresis* **2017**, *38* (20), 2592−2602.

(25) Ramshani, Z.; Zhang, C.; Richards, K.; Chen, L.; Xu, G.; Stiles, B. L.; Hill, R.; Senapati, S.; Go, D. B.; Chang, H.-C. Extracellular Vesicle Microrna Quantification from Plasma Using an Integrated Microfluidic Device. *Commun. Biol.* **2019**, *2* (1), 1−9.

(26) Davidson, S. M.; Wessling, M.; Mani, A. On the Dynamical Regimes of Pattern-Accelerated Electroconvection. *Sci. Rep.* **2016**, *6* (1), 1−10.

(27) De Valença, J.; Jõgi, M.; Wagterveld, R. M.; Karatay, E.; Wood, J. A.; Lammertink, R. G. Confined Electroconvective Vortices at Structured Ion Exchange Membranes. *Langmuir* **2018**, *34* (7), 2455−2463.

(28) Roghmans, F.; Evdochenko, E.; Stockmeier, F.; Schneider, S.; Smailji, A.; Tiwari, R.; Mikosch, A.; Karatay, E.; Kühne, A.; Walther, A.; Mani, A.; Wessling, M. 2D Patterned Ion-Exchange Membranes Induce Electroconvection. *Adv. Mater. Interfaces* **2019**, *6* (1), 1801309.

(29) Tasdelen, M. A.; Lalevée, J.; Yagci, Y. Photoinduced Free Radical Promoted Cationic Polymerization 40 Years after its Discovery. *Polym. Chem.* **2020**, *11* (6), 1111−1121.

(30) Wang, C.; Tao, Z.; Zhou, Y.; Zhao, X.; Li, J.; Ren, Q.; Guiver, M. D. Anion Exchange Membranes with Eight Flexible Side-Chain Cations for Improved Conductivity and Alkaline Stability. *Sci. China Mater.* **2020**, DOI: 10.1007/s40843-020-1432-7.

(31) Wang, C.; Tao, Z.; Zhao, X.; Li, J.; Ren, Q. Poly(aryl ether nitrile)s Containing Flexible Side-Chain-Type Quaternary Phosphonium Cations as Anion Exchange Membranes. *Sci. China Mater.* **2020**, *63* (4), 533−543.

(32) Zhou, Y.-C.; Zhou, L.; Feng, C.-P.; Wu, X.-T.; Bao, R.-Y.; Liu, Z.-Y.; Yang, M.-B.; Yang, W. Direct Modification of Polyketone Resin for Anion Exchange Membrane of Alkaline Fuel Cells. *J. Colloid Interface Sci.* **2019**, *556*, 420−431.

(33) Greaves, T. L.; Kennedy, D. F.; Mudie, S. T.; Drummond, C. J. Diversity Observed in the Nanostructure of Protic Ionic Liquids. *J. Phys. Chem. B* **2010**, *114* (31), 10022−10031.

(34) Yagci, Y.; Jockusch, S.; Turro, N. J. Photoinitiated Polymerization: Advances, Challenges, and Opportunities. *Macromolecules* **2010**, *43* (15), 6245−6260.

(35) Lin, A. A.; Sastri, V. R.; Tesoro, G.; Reiser, A.; Eachus, R. On the Crosslinking Mechanism of Benzophenone-Containing Polyimides. *Macromolecules* **1988**, *21* (4), 1165−1169.

(36) Sigal, G. B.; Bamdad, C.; Barberis, A.; Strominger, J.; Whitesides, G. M. A Self-Assembled Monolayer for the Binding and Study of Histidine-Tagged Proteins by Surface Plasmon Resonance. *Anal. Chem.* **1996**, *68* (3), 490−497.

(37) Doyen, A.; Roblet, C.; L'Archevêque-Gaudet, A.; Bazinet, L. Mathematical Sigmoid-Model Approach for the Determination of Limiting and Over-Limiting Current Density Values. *J. Membr. Sci.* **2014**, *452*, 453−459.

(38) Goksuluk, D.; Korkmaz, S.; Zararsiz, G.; Karaagaoglu, A. E. Easyroc: An Interactive Web-Tool for ROC Curve Analysis Using R Language Environment. *R Journal* **2016**, *8* (2), 213.

(39) Karas, F.; Hnát, J.; Paidar, M.; Schauer, J.; Bouzek, K. Determination of the Ion-Exchange Capacity of Anion-Selective Membranes. *Int. J. Hydrogen Energy* **2014**, *39* (10), 5054−5062.

(40) Lange, H. Determination of the Degree of Swelling and Crosslinking of Extremely Small Polymer Gel Quantities by Analytical Ultracentrifugation. *Colloid Polym. Sci.* **1986**, *264* (6), 488−493.

(41) Vargün, E.; Usanmaz, A. Part A: Pure; Chemistry, A., Degradation of Poly (2-Hydroxyethyl Methacrylate) Obtained by Radiation in Aqueous Solution. *J. Macromol. Sci., Part A: Pure Appl. Chem.* **2010**, *47* (9), 882−891.

(42) Tian, B.-H.; Fan, B.; Peng, X.-J.; Luan, Z.-K. A Cleaner Two-Step Synthesis of High Purity Diallyldimethylammonium Chloride Monomers for Flocculant Preparation. *J. Environ. Sci. (China)* **2005**, *17* (5), 798−801.

(43) Wilts, E. M.; Herzberger, J.; Long, T. E. Addressing Water Scarcity: Cationic Polyelectrolytes in Water Treatment and Purification. *Polym. Int.* **2018**, *67* (7), 799−814.

(44) Tanaka, Y. Concentration Polarization. In *Ion Exchange Membranes*, 2nd ed.; Tanaka, Y., Ed.; Elsevier: Amsterdam, 2015; pp 101−121.

(45) Kontturi, K.; Manzanares, J.; Murtomäki, L. Effect of Concentration Polarization on the Current-Voltage Characteristics of Ion Transfer Across ITIES. *Electrochim. Acta* **1995**, *40* (18), 2979−2984.

(46) Mogi, K. A Visualization Technique of a Unique pH Distribution Around an Ion Depletion Zone in a Microchannel by Using a Dual-Excitation Ratiometric Method. *Micromachines* **2018**, *9* (4), 167.

(47) Wessling, M.; Morcillo, L. G.; Abdu, S. Nanometer-Thick Lateral Polyelectrolyte Micropatterns Induce Macrosopic Electro-Osmotic Chaotic Fluid Instabilities. *Sci. Rep.* **2015**, *4*, 4294.

(48) Stodollick, J.; Femmer, R.; Gloede, M.; Melin, T.; Wessling, M. Electrodialysis of Itaconic Acid: A Short-Cut Model Quantifying the Electrical Resistance in the Overlimiting Current Density Region. *J. Membr. Sci.* **2014**, *453*, 275−281.

(49) Belloň, T.; Polezhaev, P.; Vobecká, L.; Svoboda, M.; Slouka, Z. Experimental Observation of Phenomena Developing on Ion-Exchange Systems during Current-Voltage Curve Measurement. *J. Membr. Sci.* **2019**, *572*, 607−618.

(50) Polezhaev, P.; Belloň, T.; Kurospajeva, N. C.; Vobecká, L.; Slouka, Z. Molecular Sieving of Tetraalkylammonium Cations on Cation Exchange Systems in DC Electric Field. *Sep. Purif. Technol.* **2020**, *241*, 116691.

(51) Vobecká, L.; Belloň, T.; Slouka, Z. Behavior of Embedded Cation-Exchange Particles in a DC Electric Field. *Int. J. Mol. Sci.* **2019**, *20* (14), 3579.

(52) Rubinstein, I.; Zaltzman, B. Electro-Osmotically Induced Convection at a Permselective Membrane. *Phys. Rev. E: Stat. Phys., Plasmas, Fluids, Relat. Interdiscip. Top.* **2000**, *62* (2), 2238−2251.

(53) Chang, H.-C.; Demekhin, E.; Shelistov, V. Competition Between Dukhin's and Rubinstein's Electrokinetic Modes. *Phys. Rev. E* **2012**, *86* (4), 046319.

(54) Huang, C.-J.; Lin, Z.-E.; Yang, Y.-S.; Chan, H. W.-H.; Chen, W.-Y. Neutralized Chimeric DNA Probe for Detection of Single Nucleotide Polymorphism on Surface Plasmon Resonance Biosensor. *Biosens. Bioelectron.* **2018**, *99*, 170−175.

(55) Wang, Z.-L.; Wang, H.-L.; Yan, J.-M.; Ping, Y.; O, S.-I.; Li, S.-J.; Jiang, Q. DNA-Directed Growth of Ultrafine Coaupd Nanoparticles on Graphene as Efficient Catalysts for Formic Acid Dehydrogenation. *Chem. Commun.* **2014**, *50* (21), 2732−2734.

(56) Tiwari, J. N.; Nath, K.; Kumar, S.; Tiwari, R. N.; Kemp, K. C.; Le, N. H.; Youn, D. H.; Lee, J. S.; Kim, K. S. Stable Platinum Nanoclusters on Genomic DNA−Graphene Oxide with a High Oxygen Reduction Reaction Activity. *Nat. Commun.* **2013**, *4* (1), 1−7.

(57) Vonk, R. J.; Wouters, S.; Barcaru, A.; Vivó-Truyols, G.; Eeltink, S.; De Koning, L. J.; Schoenmakers, P. J. Post-Polymerization Photografting on Methacrylate-Based Monoliths for Separation of Intact Proteins and Protein Digests with Comprehensive Two-Dimensional Liquid Chromatography Hyphenated with High-Resolution Mass Spectrometry. *Anal. Bioanal. Chem.* **2015**, *407* (13), 3817−3829.

(58) Gao, H.-L.; Zhang, H.; Li, C.-Y.; Xia, X.-H. Confinement Effect of Protonation/Deprotonation of Carboxylic Group Modified in Nanochannel. *Electrochim. Acta* **2013**, *110*, 159−163.

(59) Miller, J. *Statistics and Chemometrics for Analytical Chemistry*; Pearson Education: 2018.

■ NOTE ADDED AFTER ASAP PUBLICATION

The version of this paper that was published ASAP November 20, 2020, contained an error in Figure 13 (panel g was included, which was a duplicate of Figure 14). The paper was corrected and reposted November 23, 2020.